Supplementary Information

Stable Cycling of High-Mass Loaded MnO_2 Electrodes for Sodium-ion Batteries

Yunkai Luo,[a] Bintao Hu,[a] Swetha Chandrasekaran,[b] Megan C Freyman,[b] Dun Lin,[c] Yat Li,[c] Marcus Worsley[b] and Bruce Dunn[*a]

[a] *Department of Materials Science and Engineering, University of California, Los Angeles, California 90095, United States*
[b] *Lawrence Livermore National Laboratory, California 94550, United States*
[c] *Department of Chemistry and Biochemistry, University of California, Santa Cruz, California 95064, United States*

[*]Email: bdunn@ucla.edu

Determining the potential window for cyclic voltammetry of MnO_2

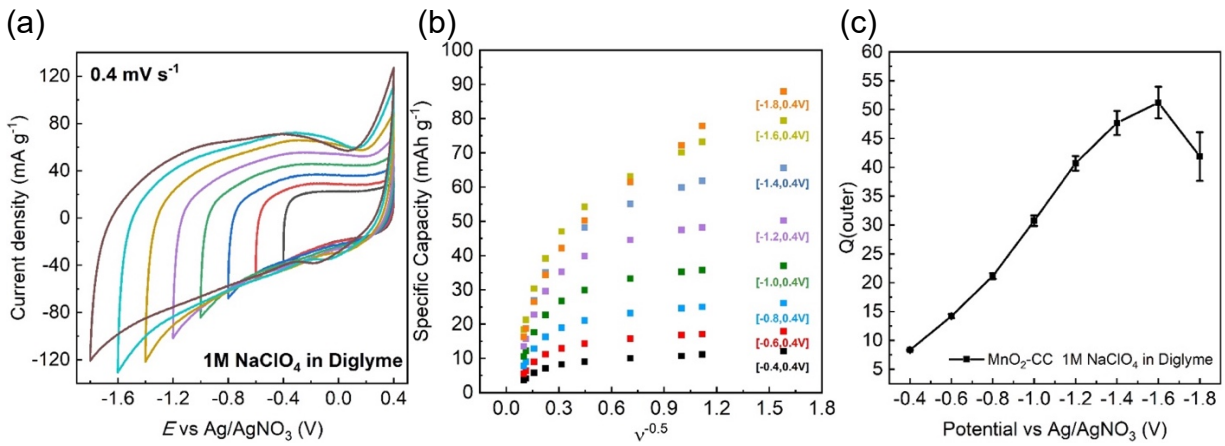

Figure S1. (a) The CV curves for MnO_2 on carbon cloth in CV potential opening experiment at a scan rate of 0.4 mV s^{-1}. (b) The specific capacity as a function of $\nu^{-0.5}$ for MnO_2 in different potential windows. (c) The fitted Q_{outer} value versus the potential.

Since MnO_2 is known to exhibit surface pseudocapacitive properties in aqueous electrolytes,[1] a cyclic voltammetry (CV) electrochemical window experiment was conducted in which the potential was varied from the aqueous potential to the potential of the non-aqueous electrolyte (**Figure S1a**).[2]The SEM images of electrodeposited MnO_2 on carbon cloth are shown in **Figure S2**, indicating a uniform coating. In addition, the Trasatti method was used to quantify electrode kinetics, as shown in **Figure S1b**.[3]

The Trasatti method, an approach for electrode kinetics analysis, separates the contribution of total charge (Q_{total}) into two components: the outer charge (Q_{outer}), independent of scan rate, and the inner charge (Q_{inner}), linked to the segment constrained by semi-infinite diffusion.[2] By extrapolating the linear fit of the reciprocal of the calculated charge against the square root of the scan rate plot, the intercept at the y-axis reveals the charge apparent at infinitely slow scan rates, signifying the total charge (Q_{total}). Similarly, by extrapolating the linear fit of the calculated charge against the reciprocal of the square root of the scan rate, the intercept at the y-axis identifies the charge independent of scan rates, denoted as the outer charge (Q_{outer}). Subtracting Q_{outer} from Q_{total} unveils the inner charge (Q_{inner}) limited by semi-infinite diffusion, where C represents the calculated capacity, and ν is the scan rate. These relationships are expressed in Equations 1 - 3.

$$C = constant \cdot \nu^{-0.5} + Q_{Outer} \quad \text{Eqn 1}$$

$$1/C = constant \cdot \nu^{0.5} + 1/Q_{Total} \quad \text{Eqn 2}$$

$$Q_{Total} = Q_{Inner} + Q_{Outer} \quad \text{Eqn 3}$$

From this analysis, comparisons of the electrode kinetics between different materials can be expressed through the ratio of Q_{outer} to Q_{total}. Since one objective for using a MnO_2 electrode is to obtain both high energy and power density, the cycling potential should be limited to the region where surface-controlled redox reactions dominate. Therefore, the Q_{outer}, was plotted versus the

potential and depicted in **Figure S1c**. The high potential end is fixed to avoid having oxygen evolution reaction.[4]The Q_{outer} initially increases when the potential gradually approaches the lower value. It is found that when the cycling potential is below -1.4 V, the Q_{outer} stops increasing and reaches a plateau, which implies the capacity contribution beyond this limit is mainly from the diffusion of ions into the bulk MnO_2. Thus, to simultaneously obtain both high capacity and good electrode kinetics, the discharge potential should be limited to -1.4 V.

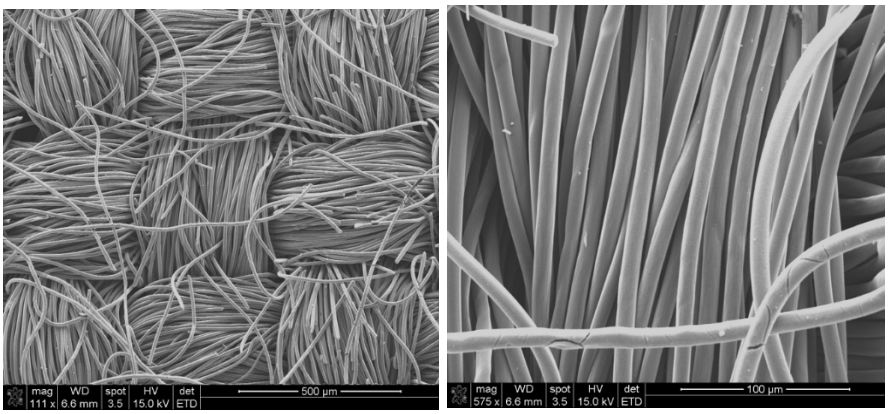

Figure S2. The SEM images of MnO_2 on carbon cloth.

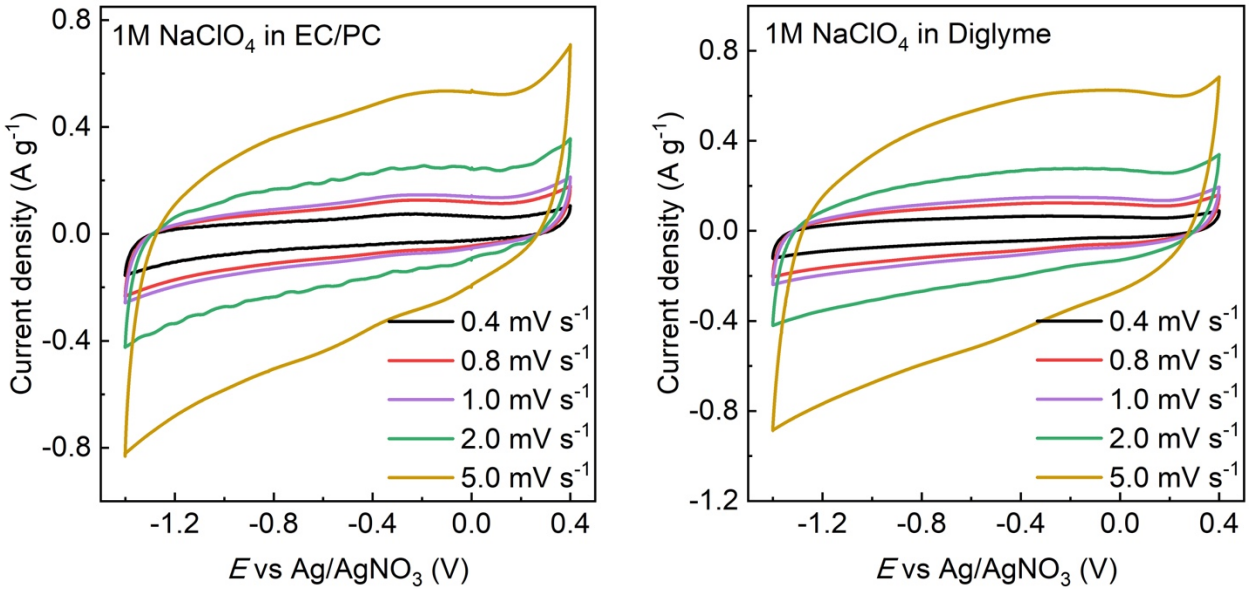

Figure S3. (a) CV curves for MnO_2 on carbon cloth in 1M $NaClO_4$ in EC/PC from the scan rate of 0.4 mV s^{-1} to 5 mV s^{-1}. (b) CV curves for MnO_2 on carbon cloth in 1M $NaClO_4$ in diglyme from the scan rate of 0.4 mV s^{-1} to 5 mV s^{-1}.

Determining the potential window for EQCM measurements

The electrode kinetics of MnO_2 were evaluated by using the Trasatti method, which is shown in **Figure S4**.[3]In the potential window of -0.4 V to 0.4 V, the capacitive capacity to total capacity ratio is similar in diglyme and PC electrolyte, which implies a similar surface reaction-dominated charge storage mechanism. Compared to the potential window of -1.4 V to 0.4 V, the electrode kinetics of MnO_2 in diglyme electrolyte are significantly different from that in PC electrolyte. The redox reaction of MnO_2 that occurred in PC electrolyte included the diffusion of sodium ions into bulk MnO_2, where the mass change of electrode in EQCM test is hard to differentiate. Thus, the potential window of -0.4 V to 0.4 V was chosen for EQCM measurements for MnO_2 in both electrolytes.

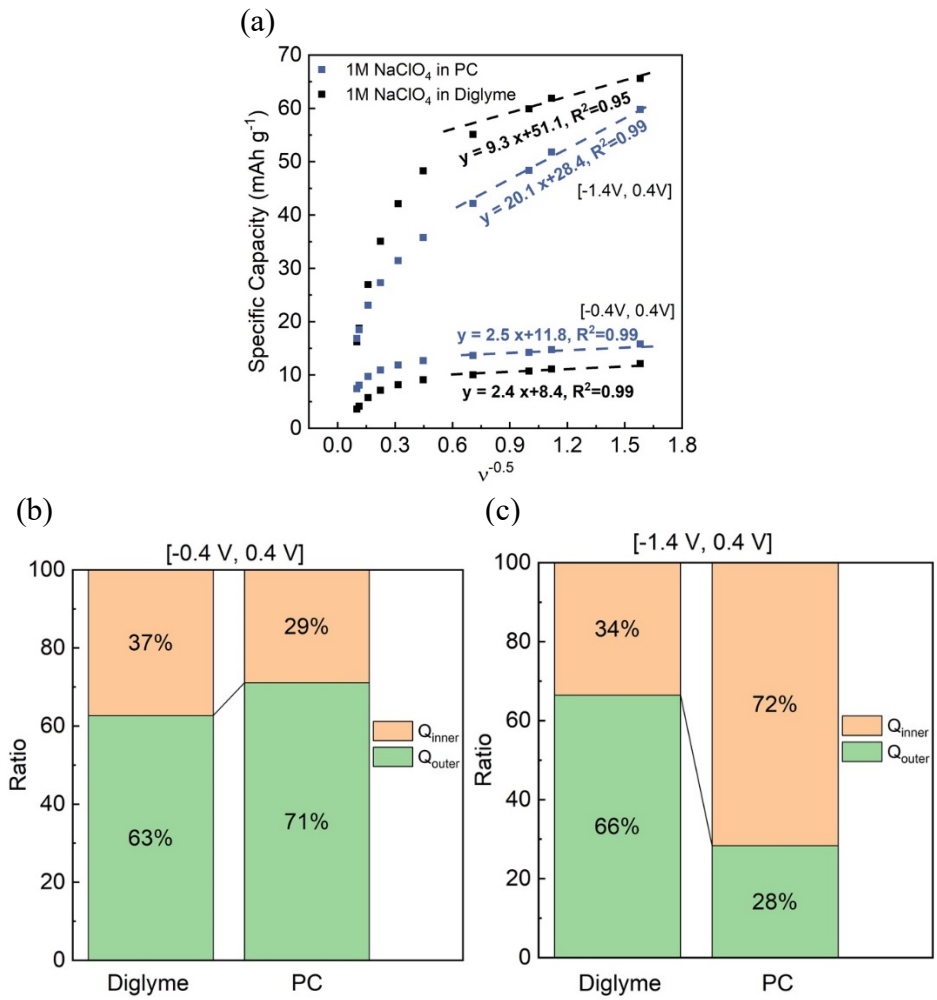

Figure S4. (a) The specific capacity as a function of $v^{-0.5}$ for MnO_2 on carbon cloth in PC and diglyme electrolyte for two different potential windows: -0.4 V to 0.4 V and -1.4 V to 0.4 V. (b) The relative ratio of Q_{outer} and Q_{inner} in MnO_2 on carbon cloth in -0.4 V to 0.4 V potential window

for both PC and diglyme electrolyte. (c) The relative ratio of Q_{outer} and Q_{inner} in MnO_2 on carbon cloth in -1.4 V to 0.4 V potential window for both PC and diglyme electrolyte.

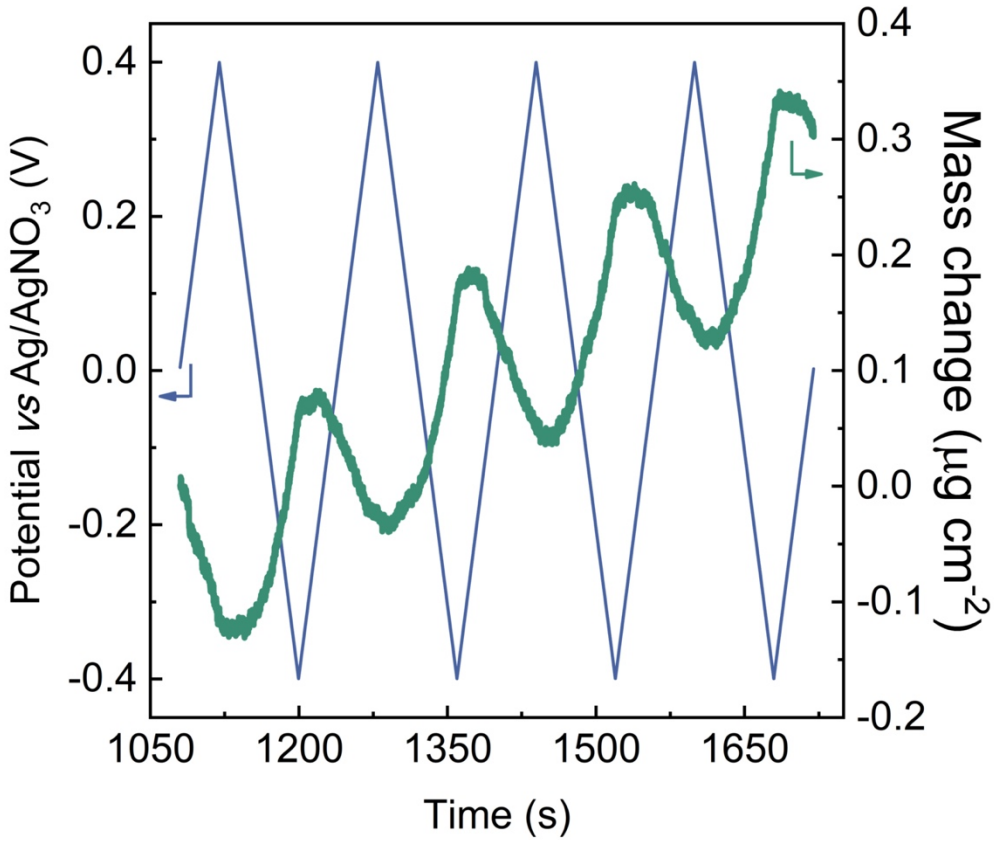

Figure S5. Potential versus time with corresponding mass change information for MnO_2 cycling in diglyme electrolyte in the EQCM measurement. Results are shown for cycle 3 to cycle 6 during CV measurement at a scan rate of 10 mV s^{-1}.

(a) (b) (c)

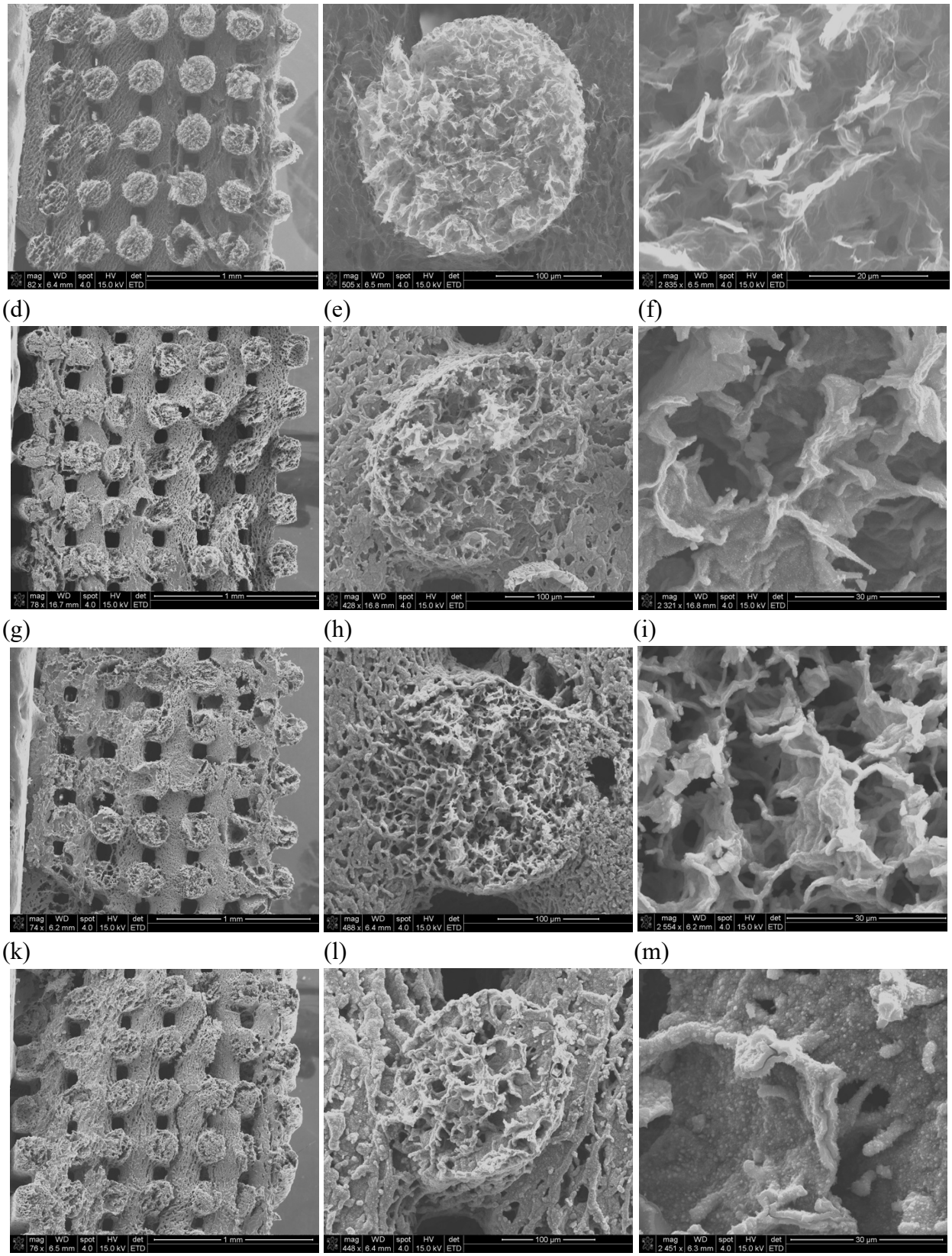

Figure S6. (a) to (c) The cross-section SEM images of 3D GA. (d) to (f) The cross-section SEM images of 21.6 mg cm^{-2} MnO_2/GA electrode. (g) to (i) The cross-section SEM images of 37.4 mg

cm^{-2} MnO_2/GA electrode. (k) to (m) The cross-section SEM images of 57.2 mg cm^{-2} MnO_2/GA electrode

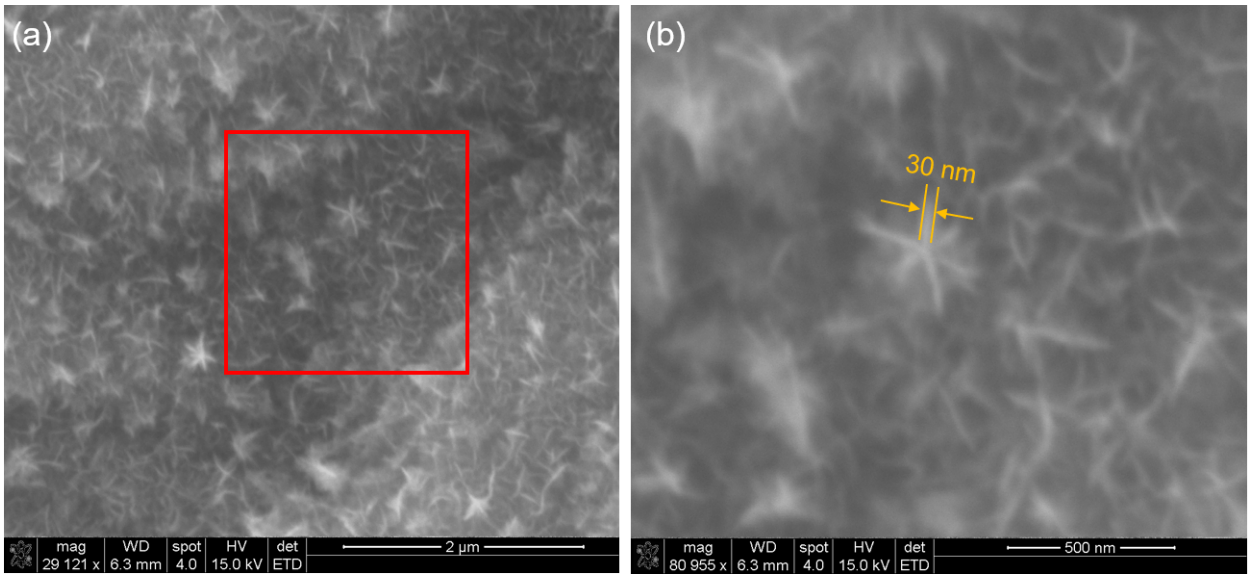

Figure S7. (a) The planar view SEM image of 21.6 mg cm^{-2} MnO_2/GA electrode and morphology of deposited MnO_2. (b) The magnified image of the red rectangle in Figure S7(a).

(a)

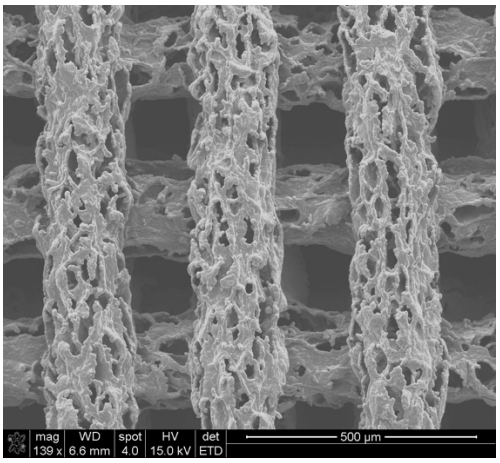
mag
139 x
WD
6.6 mm
spot
4.0
HV
15.0 kV
det
ETD
500 µm

(b)

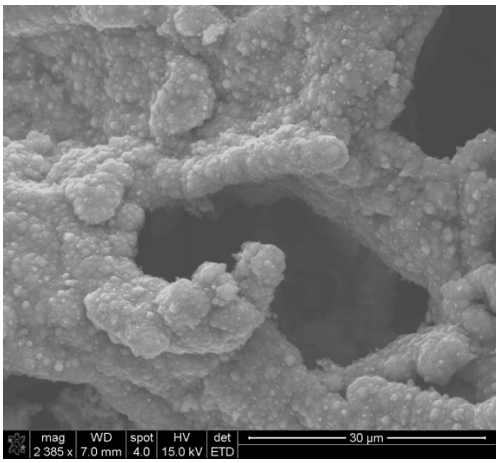
mag
2 385 x
WD
7.0 mm
spot
4.0
HV
15.0 kV
det
ETD
30 µm

(c)

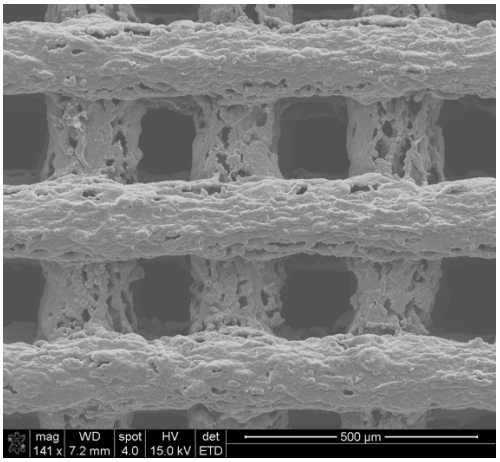
mag
141 x
WD
7.2 mm
spot
4.0
HV
15.0 kV
det
ETD
500 µm

(d)

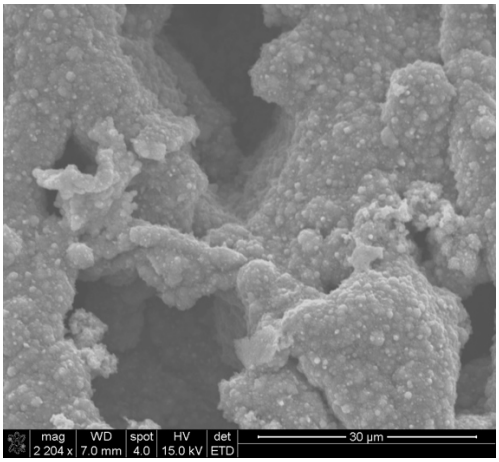
mag
2 204 x
WD
7.0 mm
spot
4.0
HV
15.0 kV
det
ETD
30 µm

(e)

(f)

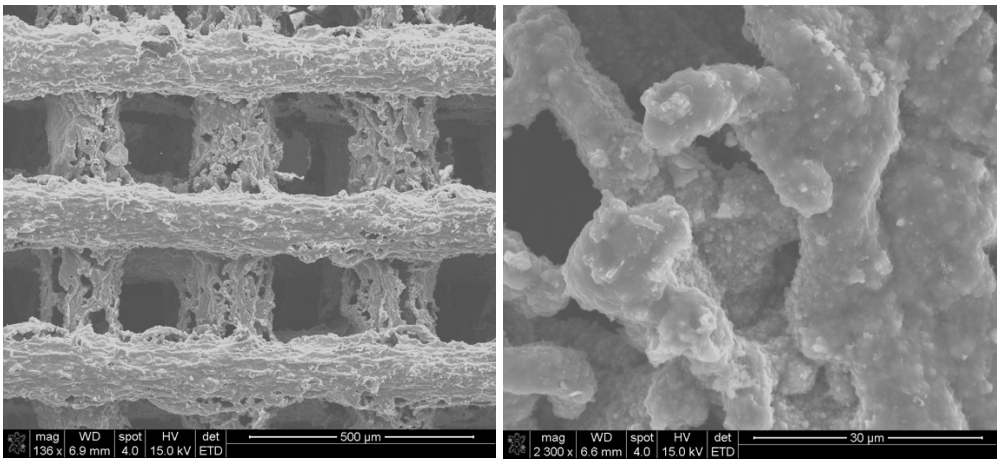

Figure S8. (a), (b) The planar view SEM images of 21.6 mg cm^{-2} MnO_2/GA electrode. (c), (d) The planar view SEM images of 37.4 mg cm^{-2} MnO_2/GA electrode. (e), (f) The planar view SEM images of 57.2 mg cm^{-2} MnO_2/GA electrode.

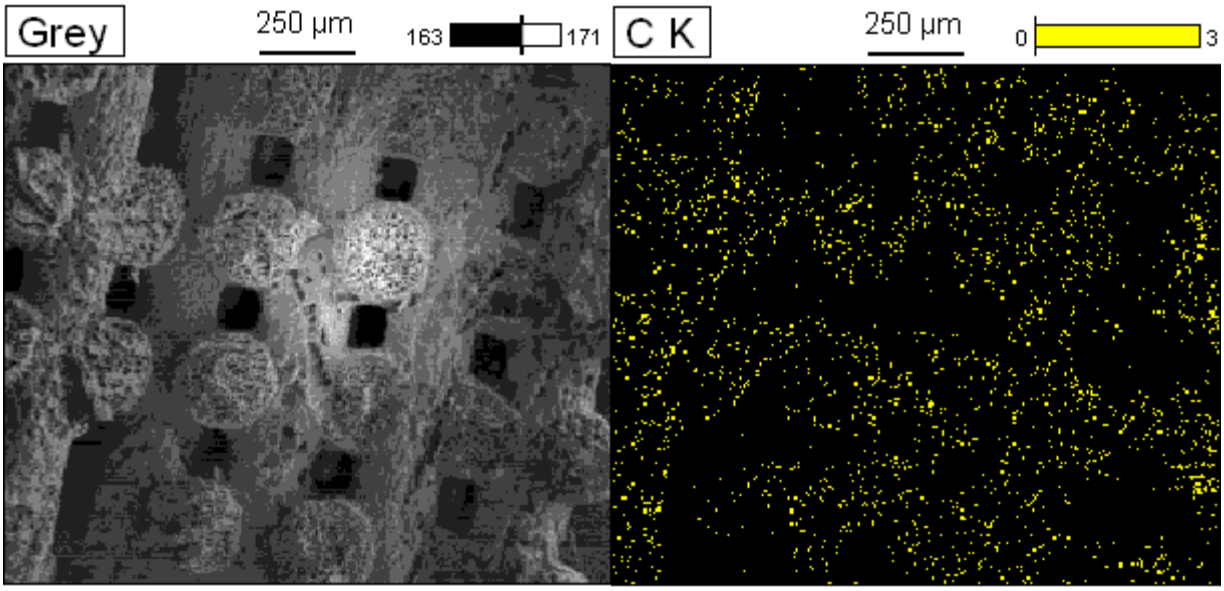

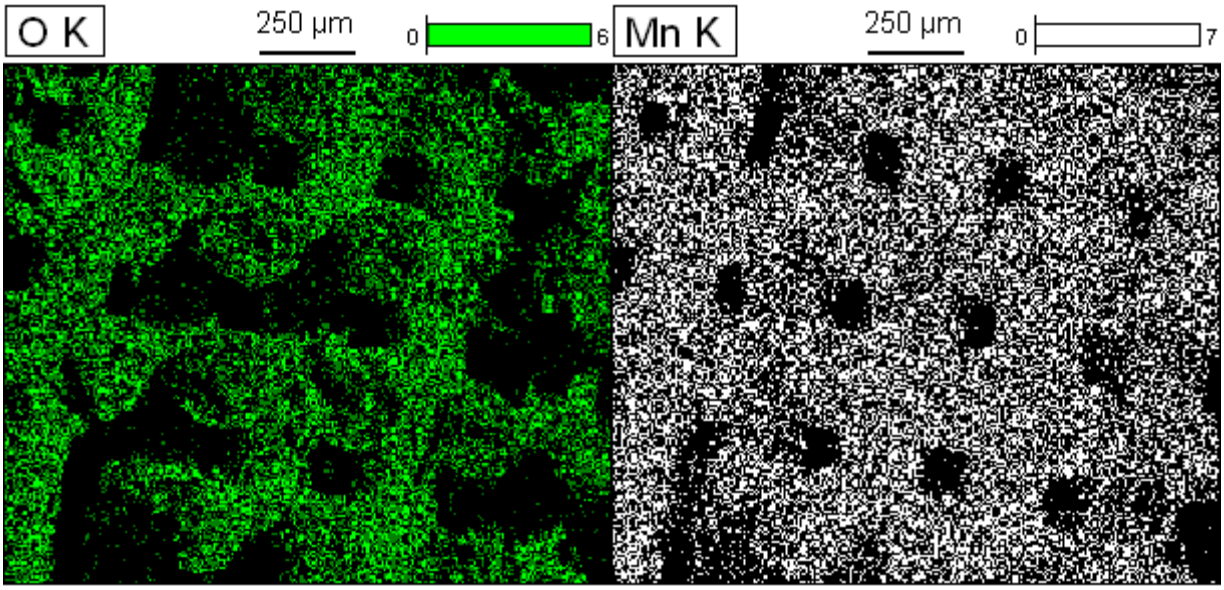

Figure S9. The EDX elemental analysis of 79.6 mg cm^{-2} MnO_2/GA electrode.

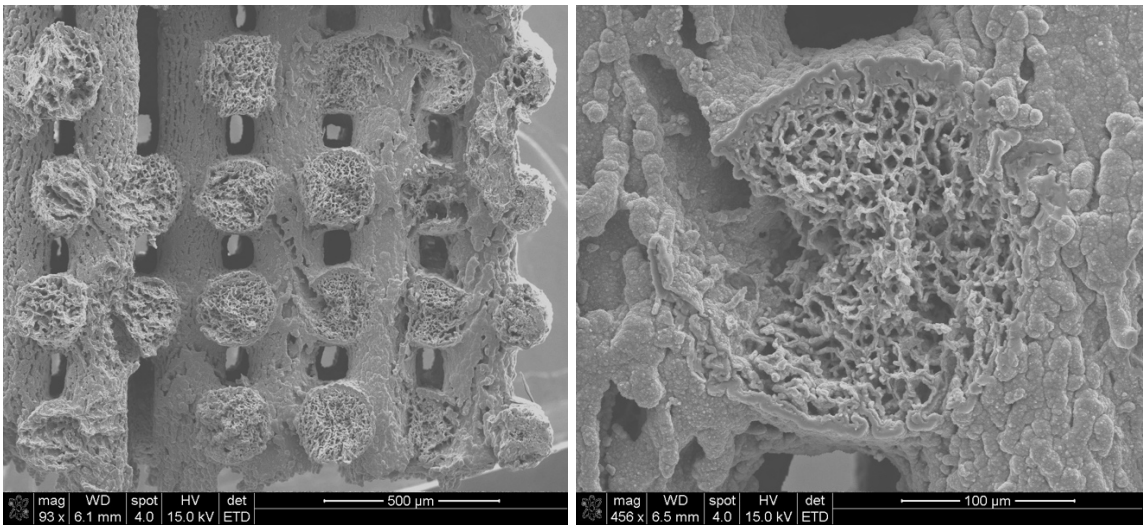

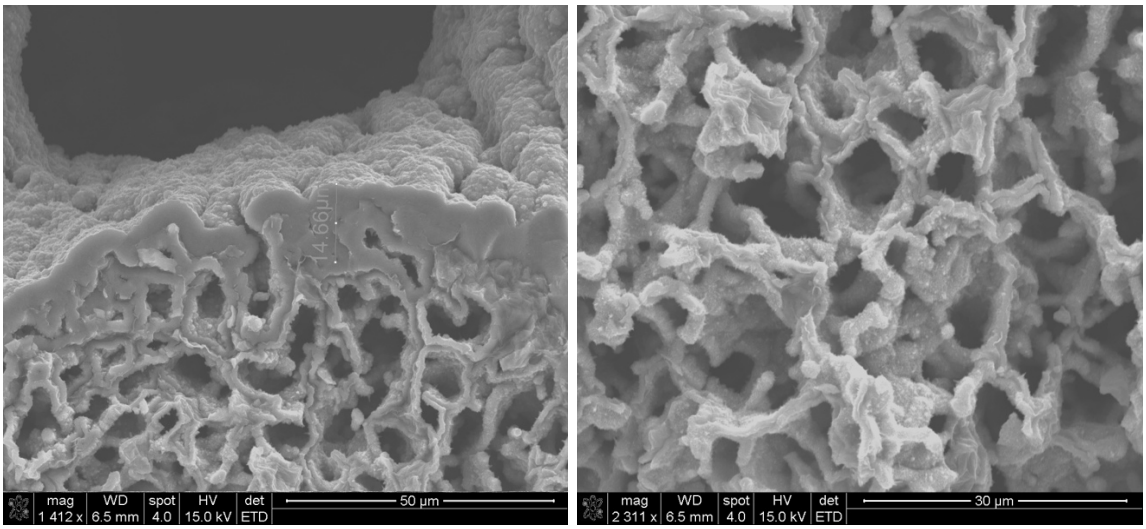

Figure S10. The cross-section SEM images of 79.6 mg cm^{-2} MnO_2/GA electrode and magnified images of the dense and thick MnO_2 shell.

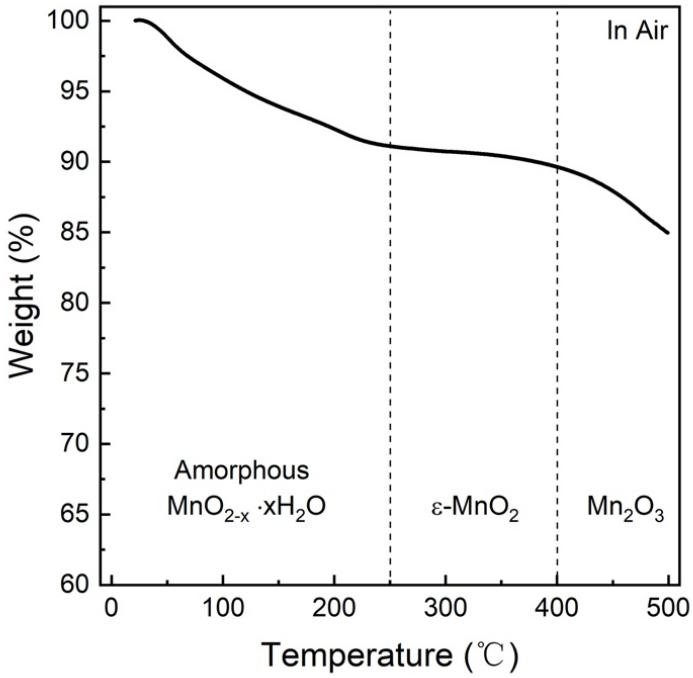

Figure S11. Thermogravimetric analysis showing weight loss as a function of temperature for as-deposited MnO_x heated from 20 ℃ to 500 ℃ in air. The phase changes occurring over this temperature range are indicated.

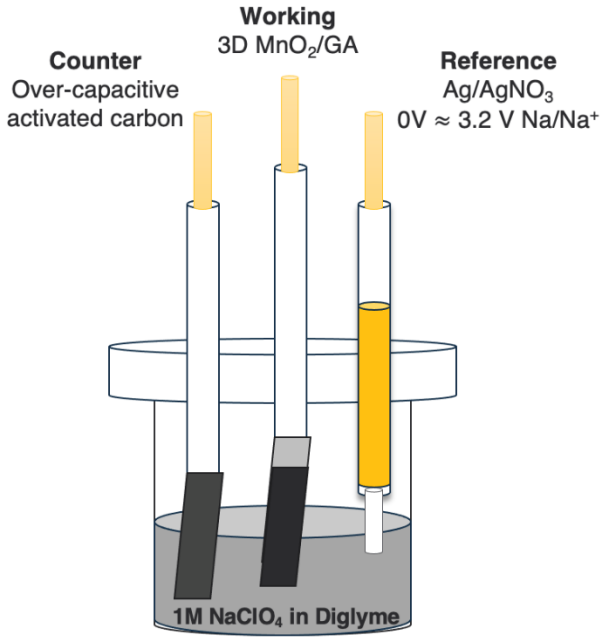

Figure S12. Schematic of the three electrode setup for conducting electrochemical tests.

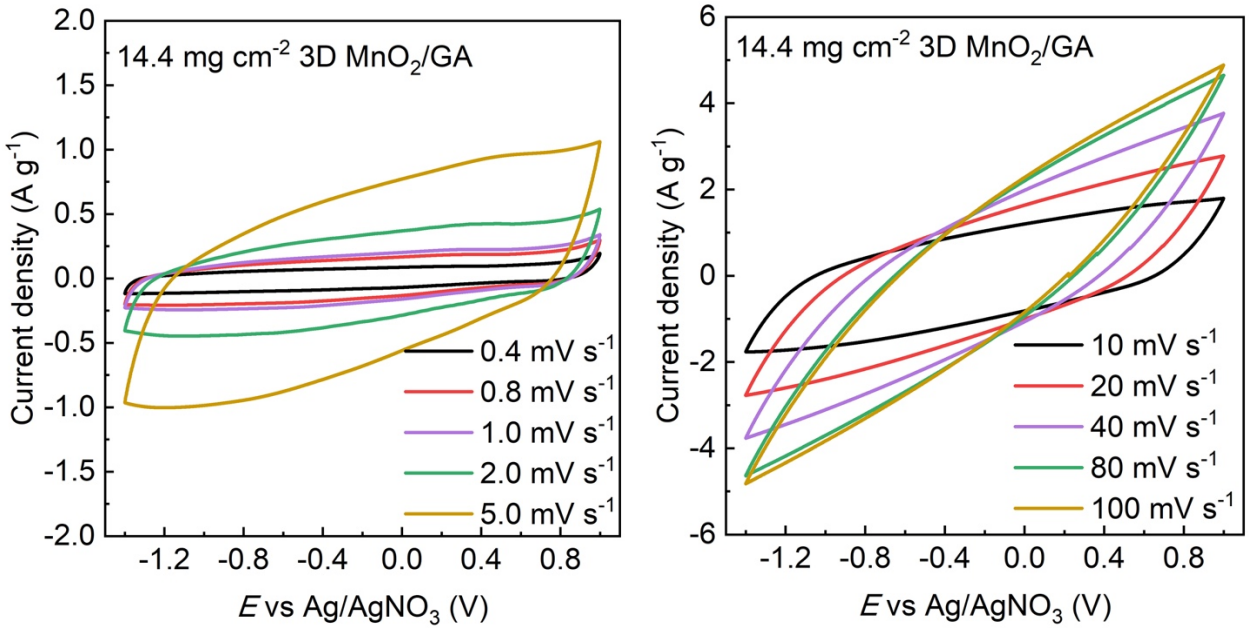

Figure S13. The CV curves for 14.4 mg cm^{-2} MnO_2/GA electrode from a scan rate of 0.4 mV s^{-1} to 5 mV s^{-1} (left) and from a scan rate of 10 mV s^{-1} to 100 mV s^{-1} (right).

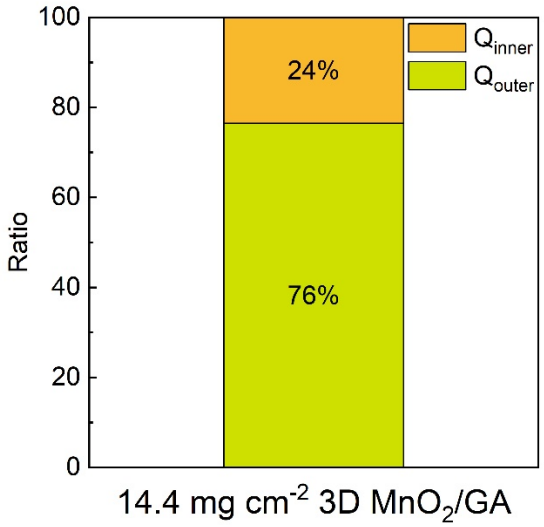

Figure S14. The relative ratio of Q_{outer} and Q_{inner} in 14.4 mg cm^{-2} 3D MnO_2/GA by using Trasatti method analysis.

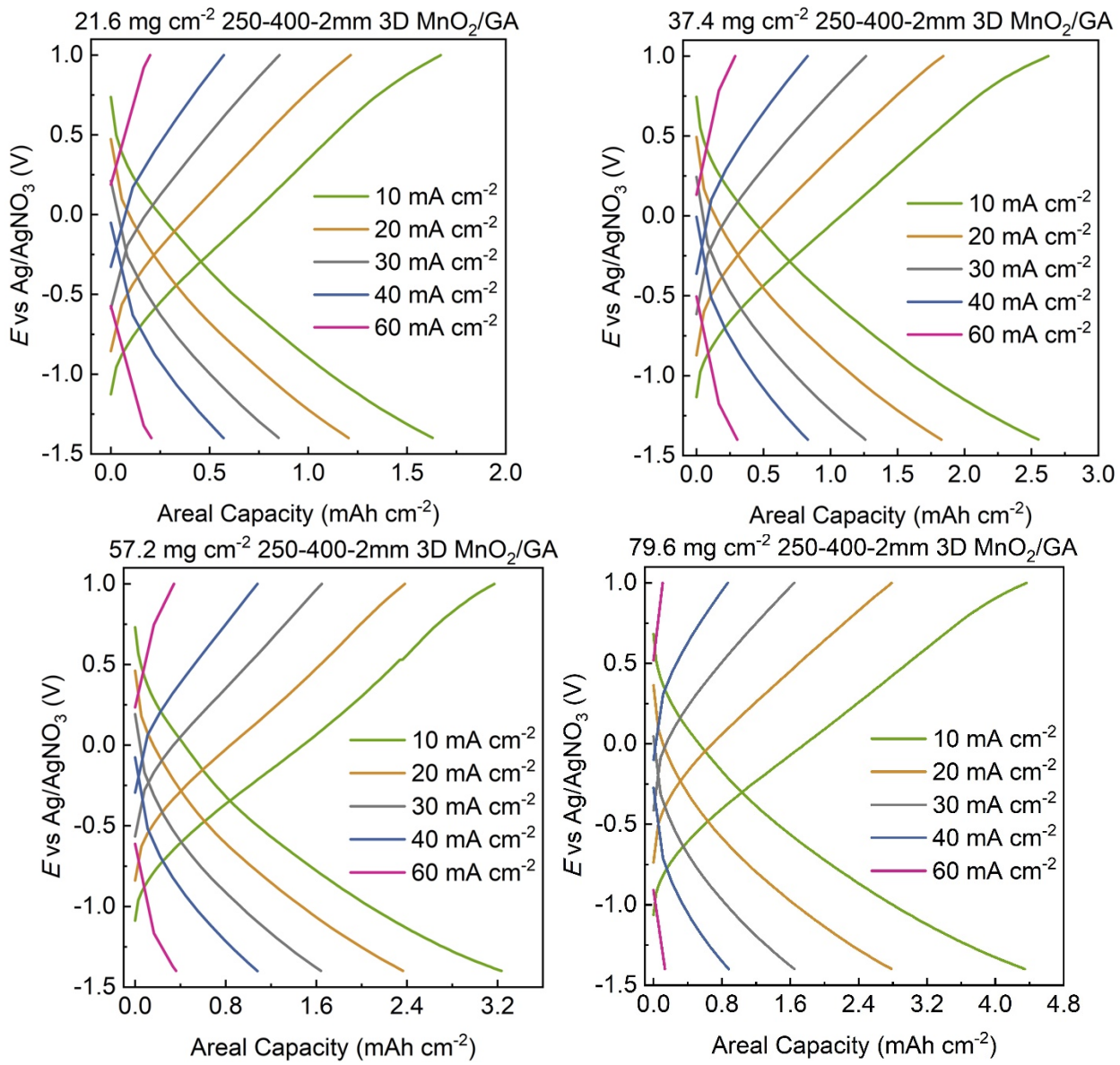

Figure S15. GV curves for 21.6 mg cm^{-2}, 37.4 mg cm^{-2}, 57.2, and 79.6 mg cm^{-2} MnO_2/GA electrodes from current densities of 10 mA cm^{-2} to 60 mA cm^{-2}.

Determining the overpotential.

The overpotential (η) were determined by using the high-end voltage (1 V vs $Ag/AgNO_3$) subtracted from the onset voltage during the constant current discharging process, as described in the equation below:

$$\eta = 1 - V_{discharge-onset}\ (V)$$

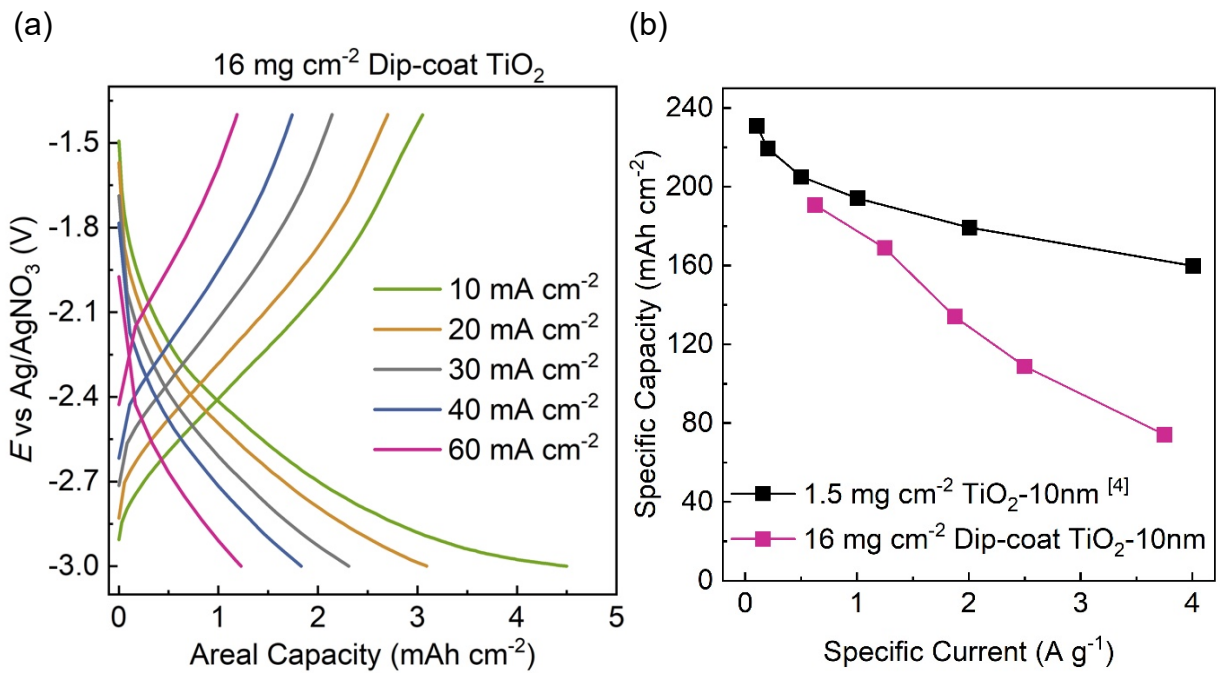

Figure S16. (a) The GV curve for dip-coated a-TiO_2 anode for current densities of 10 mA cm^{-2} to 60 mA cm^{-2}. (b) The electrochemical performance comparison between dip-coat a-TiO_2 with tape-cast a-TiO_2 electrode.[5]

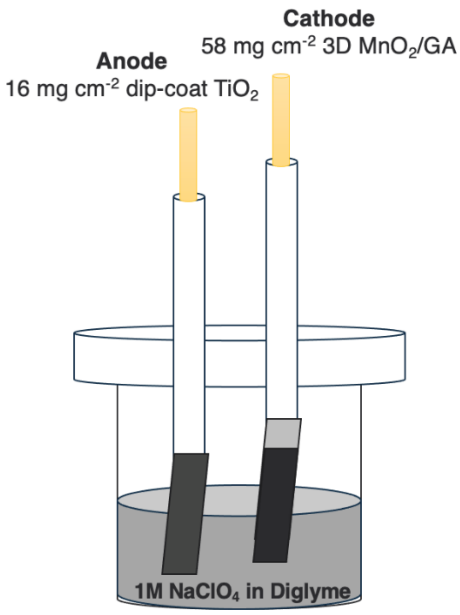

Figure S17. The two electrode set up for characterizing the SIB device in a beaker cell.

Reference

1. J. Cao, X. Li, Y. Wang, F. C. Walsh, J.-H. Ouyang, D. Jia and Y. Zhou, *J. Power Sources* 2015, **293**, 657.

2. R. Vincent, Y. Luo, J. Andrews, A. Zohar, Y. Zhou, Q, Yan. E. Mozur, M. Preefer, J. Weker, A. Cheetham, J. Luo, L. Pilon, B. Melot, B. Dunn and R. Seshadri, *Chem. Mater.* 2022, **34**, 9, 4122–4133

3. S. Ardizzone, G. Fregonara and S. Trasatti, *Electrochim. Acta* 1990, **35**, 263.

4. D. Huang, S. Li, X. Zhang, Y. Luo, J. Xiao and H. Chen, *Carbon* 2018, **129**, 468.

5. Q. Wei, X. Chang, D. Butts, R. DeBlock, K. Lan, J. Li, D. Chao, D. L. Peng and B. Dunn, *Nat. Commun.* 2023, **14**, 7.